

# Precious Metal-Free $\text{LaMnO}_3$ Perovskite Catalyst with an Optimized Nanostructure for Aerobic C–H Bond Activation Reactions: Alkylarene Oxidation and Naphthol Dimerization

Yesim Sahin, Abel T. Sika-Nartey, Kerem E. Ercan, Yusuf Kocak, Sinem Senol, Emrah Ozensoy,\* and Yunus E. Türkmen\*



Cite This: *ACS Appl. Mater. Interfaces* 2021, 13, 5099–5110



Read Online

ACCESS |



Metrics & More



Article Recommendations



Supporting Information

**ABSTRACT:** In this article, we describe the development of a new aerobic C–H oxidation methodology catalyzed by a precious metal-free  $\text{LaMnO}_3$  perovskite catalyst. Molecular oxygen is used as the sole oxidant in this approach, obviating the need for other expensive and/or environmentally hazardous stoichiometric oxidants. The electronic and structural properties of the  $\text{LaMnO}_3$  catalysts were systematically optimized, and a reductive pretreatment protocol was proved to be essential for acquiring the observed high catalytic activities. It is demonstrated that this newly developed method was extremely effective for the oxidation of alkylarenes to ketones as well as for the oxidative dimerization of 2-naphthol to 1,1-binaphthyl-2,2-diol (BINOL), a particularly important scaffold for asymmetric catalysis. Detailed spectroscopic and mechanistic studies provided valuable insights into the structural aspects of the active catalyst and the reaction mechanism.

**KEYWORDS:** alkylarenes, C–H oxidation, heterogeneous catalysis, perovskites, surface chemistry



## INTRODUCTION

In the past two decades, catalytic functionalization of unactivated C–H bonds has attracted broad attention across various fields of chemistry as it presents a profound potential to change the way we think about chemical synthesis.<sup>1–7</sup> In this respect, C–H oxidation reactions constitute an important subclass of such C–H functionalization reactions where unactivated  $\text{CH}_x$  groups are generally oxidized to value-added alcohols or carbonyl-containing functional groups.<sup>8–11</sup> Among the various catalytic processes developed for C–H oxidation reactions, those that involve nonprecious, earth-abundant transition-metal salts or complexes as catalysts and molecular oxygen as the stoichiometric oxidant are particularly attractive from an environmental as well as an economical perspective.<sup>8,12–17</sup>

Since their discovery by German mineralogist Gustav Rose in 1839,<sup>18</sup> perovskites with a general formula unit of  $\text{ABO}_3$  have received significant attention in chemistry and physics.<sup>18–22</sup> Particularly, by virtue of their structural tunability allowing modification of their A-site and B-site cations, oxygen vacancy contents, crystal defect types, and defect densities, perovskites have proven to demonstrate unique magnetic, electronic, and catalytic functionalities.<sup>18–23</sup>

In the quest to minimize the use of precious platinum group metal (PGM, e.g., Pt, Pd, Rh, Ir, etc.)-based catalysts, perovskites

have been frequently utilized in heterogeneous catalytic organic reactions as fine-tunable and versatile catalytic materials.<sup>19,24,25</sup> Perovskites have also been demonstrated by the Hara and Kamata groups to be effective heterogeneous catalysts in a variety of oxidation reactions.<sup>26–29</sup> In recent years, lead-halide perovskites have also been reported to be promising photocatalysts for various organic reactions involving C–C, C–N, and C–O bond formation.<sup>30,31</sup> While thermal catalytic (i.e., nonphotocatalytic) aerobic oxidation of alcohols has been frequently studied in the literature,<sup>32</sup> there exist only a few studies investigating aerobic oxidation of alkylarenes.<sup>33</sup> This may be partly because of the more challenging nature of the alkylarenes associated with their higher homolytic C–H bond dissociation energies as compared to those of alcohols.<sup>34</sup> Thus, in the current work, we demonstrate how precious metal-free perovskites (e.g.,  $\text{LaMnO}_3$ ) can be structurally optimized to efficiently catalyze not only the aerobic oxidation of alkylarenes

Received: November 17, 2020

Accepted: January 11, 2021

Published: January 25, 2021



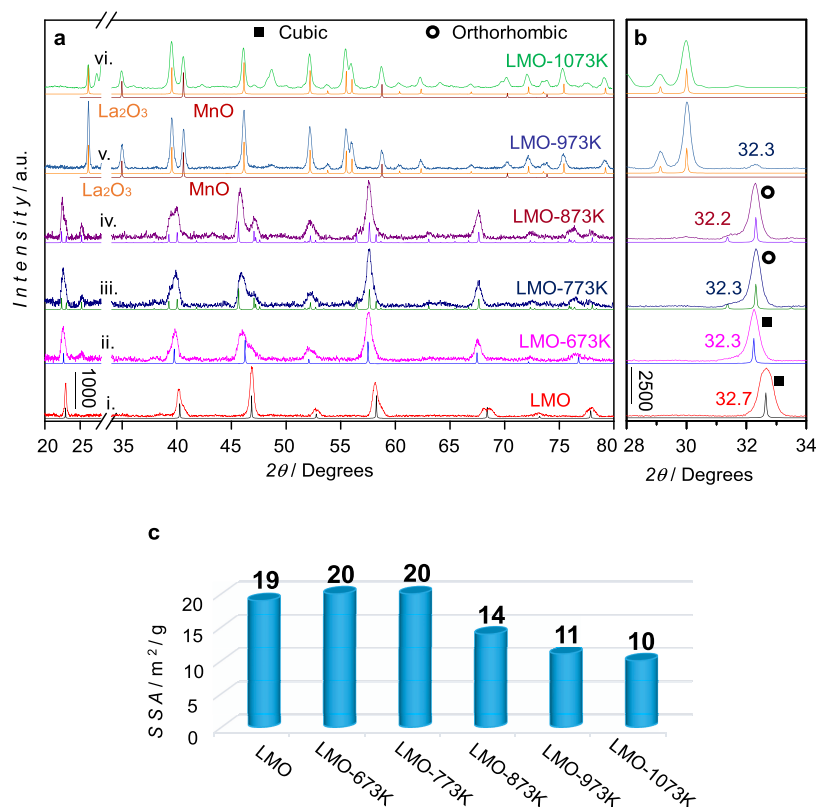


**Figure 1.** (a) XRD profiles of (i) LMO (PDF Card No. 04-013-9804), (ii) LMO-673K (PDF Card No. 04-006-9580), (iii) LMO-773K (PDF Card No. 04-006-9581), (iv) LMO-873K (PDF Card No. 04-006-9581), (v) LMO-973K (MnO PDF Card No. 04-002-5617 and La<sub>2</sub>O<sub>3</sub> PDF Card No. 04-008-7342), and (vi) LMO-1073K (MnO PDF Card No. 04-002-5617 and La<sub>2</sub>O<sub>3</sub> PDF Card No. 04-008-7342). Diffractograms given below the experimental data are the corresponding reference XRD data. (b) Detailed views of the XRD patterns for 28° < 2θ < 34°. (c) Brunauer–Emmett–Teller (BET) specific surface area (SSA) values of fresh and reduced LMO catalysts.

to ketones but also aerobic oxidative dimerization of naphthols to obtain 1,1'-binaphthyl-2,2'-diol (BINOL) derivatives.

## RESULTS AND DISCUSSION

**Catalyst Characterization.** The LaMnO<sub>3</sub> (LMO)-based perovskite catalyst was synthesized as described in Experimental Section. Next, the electronic and structural properties of the fresh perovskite were gradually modified in a controlled manner *via* a reduction protocol carried out within 673–1073 K. Modified catalysts were named LMO-*X*, where *X* stands for the particular temperature used in the reduction protocol.

X-ray diffraction (XRD) patterns of the unreduced and reduced LMO catalysts are shown in Figure 1a. Well-defined XRD signals of the unreduced LMO catalyst indicate that LMO has a characteristic cubic perovskite structure with a relatively smaller lattice parameter evident by the major diffraction signal located at a large 2θ value of 32.7°. Structural properties of the unreduced LMO catalyst were also investigated in detail *via* X-ray absorption near-edge spectroscopy (XANES) as well as extended X-ray absorption fine structure (EXAFS) techniques (See Supporting Information, SI Section S1). Current EXAFS results (Figure S1a,b) are also in particularly good agreement with the presence of a cubic perovskite crystal structure for the LMO catalyst. Furthermore, associated XANES (Figure S1c) data also reveal that the average bulk oxidation state of the catalytically active<sup>35–37</sup> B-site cations (i.e., Mn<sup>*x*+</sup>) is greater than +3 (i.e., +3 < *x* < +4). In other words, prominent bulk oxidation states of the catalytically active B-site cations in the LMO structure are likely to be Mn<sup>3+</sup> and Mn<sup>4+</sup>, where the presence of

minority Mn<sup>2+</sup> species cannot be ruled out. These observations are in line with the former studies, suggesting that LMO typically exhibits an oxygen-surplus bulk stoichiometry in the form of LaMnO<sub>3+δ</sub>.<sup>38,39</sup> Thus, starting with this oxygen-surplus bulk stoichiometry, reduced LMO structures with various amounts of oxygen vacancies can be readily prepared.

XRD data presented in Figure 1b shows that as a result of reduction within 673–873 K and associated structural modification, major perovskite diffraction feature of LMO shifts to a lower 2θ value (i.e., 32.2°), indicating an expansion in the unit cell size. This behavior can be attributed to the reduction of the B-site Mn cations, formation of oxygen vacancies, and the change in the ionic radius of the B-site cation, as will be discussed in more depth in the forthcoming sections. Figure 1a,b also reveals that increasing reduction temperature alters the crystal structure of the perovskite domains from a cubic (300–673 K) to an orthorhombic (773 K) polymorph. Furthermore, extreme reduction at *T* ≥ 973 K leads to additional profound changes, resulting in the loss of the structural integrity of the perovskite and formation of separate La<sub>2</sub>O<sub>3</sub> and MnO phases. On the other hand, the presence of a small but detectable diffraction feature at 32.3° for the LMO-973K sample suggests that LaMnO<sub>3</sub> domains still exist as minority species after reduction at 973 K. XRD data given in Figure 1a,b demonstrate that the bulk crystal structure of the currently synthesized LaMnO<sub>3</sub> catalysts can be modified in a controlled manner *via* reduction at elevated temperatures. It is important to emphasize that the catalyst with the highest catalytic performance investigated in the current study is LMO-873K, which reveals

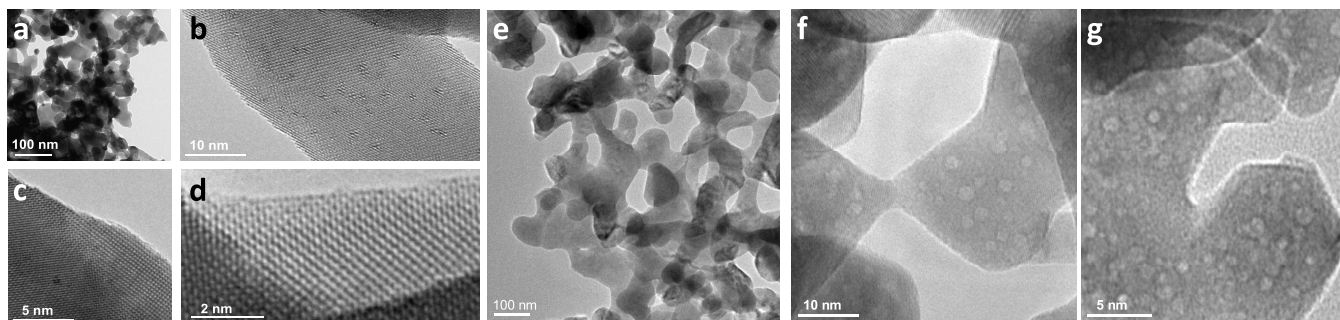


**Figure 2.** (a–d) TEM images of unreduced LMO catalysts. (e–g) TEM images of the reduced LMO-873K catalyst.

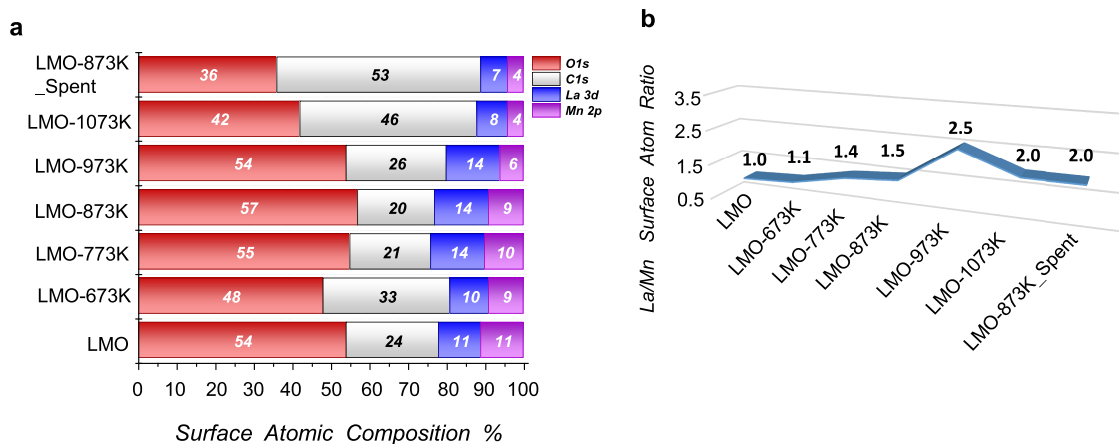


**Figure 3.** (a) Surface atomic composition percentiles and (b) La/Mn surface atom ratio for the LMO catalyst and its reduced forms at various temperatures (i.e., 673–1073 K) as well as for the spent LMO-873K catalyst that was obtained after xanthene oxidation *via* XPS (see the text for details).

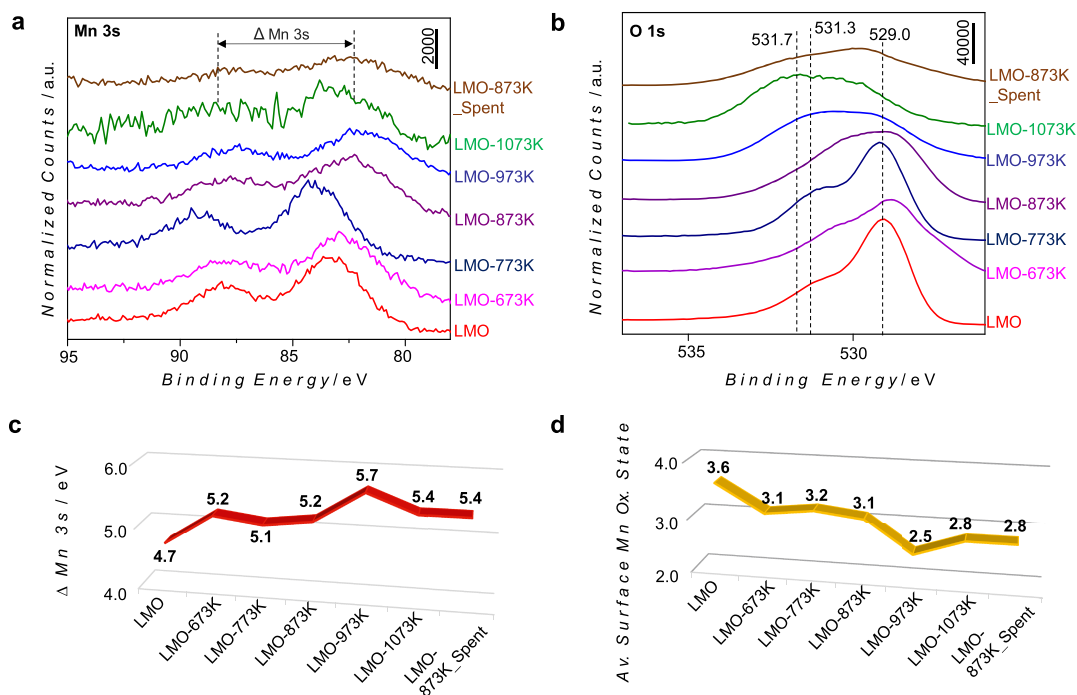


**Figure 4.** (a) Mn 3s and (b) O 1s XPS spectra, (c) binding energy splitting values of the Mn 3s signals ( $\Delta$ Mn 3s), and (d) average oxidation state of surface Mn species of the LMO catalyst and its reduced forms at various temperatures (i.e., 673–1073 K) as well as for the spent LMO-873K catalyst that was obtained after xanthene oxidation (see the text for details).

a unique orthorhombic crystal structure, exhibiting additional characteristic morphological, electronic, and stoichiometric properties, which will be discussed below.

Figure 1c shows that the specific surface area (SSA) values of the modified LMO catalysts also change as a result of the reduction protocol, in good agreement with the corresponding crystallographic changes suggested by the current XRD data (Figure 1a,b). It is apparent that while SSA values remain rather invariant within 300–773 K, a significant fall in SSA is observed after reduction at 873 K, possibly due to sintering of the perovskite crystallites and ordering of the orthorhombic lattice structure (Figure 1c). Furthermore, transformation of the perovskite structure into two separate phases (i.e.,  $\text{La}_2\text{O}_3$  and MnO) at  $T \geq 973$  K leads to an additional significant drop in SSA. Along these lines, the best performing catalyst (LMO-873K) possesses a moderate SSA value of  $14 \text{ m}^2/\text{g}$ , which lies between that of the unreduced LMO catalyst ( $19 \text{ m}^2/\text{g}$ ) and the severely reduced LMO-1073K catalyst ( $10 \text{ m}^2/\text{g}$ ).

Low-magnification transmission electron microscopy (TEM) image of the unreduced LMO catalyst given in Figure 2a shows perovskite crystallites with diameters ranging within 20–40 nm, while the higher-magnification TEM images shown in Figure 2b–d clearly confirm the crystallinity and the high structural order of the unreduced LMO sample, in good accordance with the corresponding well-defined XRD signals observed in Figure 1a,b. Interestingly, TEM images (Figure 2e–g) of the best performing perovskite (i.e., LMO-873K) reveal significant morphological differences as compared to those of the unreduced LMO catalyst. As can be seen in Figure 2f,g, upon reduction, the LMO-873K catalyst shows a relatively less uniform structure and exhibits new domains with a typical diameter of ca. 2–3 nm heterogeneously dispersed over the LMO-873K catalyst.

In an attempt to examine the variations in the surface elemental composition of the LMO catalysts as a function of reduction temperature, we performed X-ray photoelectron spectroscopy (XPS) experiments. Figure 3a,b shows the corresponding surface atomic composition % values derived from the current XPS data given in Figures 4 and S2. It is important to note that as an implication of the citrate method utilized in catalyst synthesis, significant amounts of residual C and O were observed to be present on all catalyst surfaces (Figure 3a), rendering the surface C/O elemental analysis rather complicated. Thus, here, we avoid detailed quantitative analysis of the surface C and O atom contents of the catalysts. In spite of this constraint, valuable semiquantitative insight can be still obtained from the results presented in Figure 3a,b. First, for the unreduced LMO catalyst, surface atomic contents of La and Mn are observed to be rather comparable, which is in accordance with the general  $\text{ABO}_3$  perovskite stoichiometry, suggesting similar A-site (La) and B-site (Mn) cation contents. Accordingly, surface oxygen concentrations of the catalysts are typically greater than their corresponding La and Mn concentrations by a factor of ca. 4–5, which is also fairly consistent with a perovskite structure. Note that residual  $-\text{CO}_x$ ,  $-\text{OH}$ , and  $-\text{C}_x\text{H}_y\text{O}_z$  surface species also possibly have a contribution to the measured surface O atom content of the catalysts. Second, when the La/Mn surface atomic concentration ratio is investigated as a function of the increasing extent of reduction (Figure 3b), it is seen that the LMO surface composition constantly changes and the catalyst surfaces are monotonically enriched with La with increasing reduction temperatures up to 973 K. Particularly, La enrichment exhibits a

drastic boost at 973 K, which is in line with the XRD data given in Figure 1a,b indicating the destruction of the perovskite lattice and formation of a predominant  $\text{La}_2\text{O}_3$  phase with intense XRD signals. It is apparent that after reduction at 973 K, the  $\text{La}_2\text{O}_3$  phase reveals higher dispersion on the surface in contrast to the MnO phase, where the latter phase suffers from agglomeration or is partially covered with  $\text{La}_2\text{O}_3$ , leading to lower Mn XPS signal intensities. These results point out to the fact that in addition to the bulk crystallographic changes evident by the current XRD results (Figure 1a,b) as well as the morphological changes observed in TEM images (Figure 2a–g), the reduction protocol also induces significant surface compositional modifications in the reduced LMO catalysts (Figure 3a,b).

Further insight into the electronic structural changes occurring on the LMO catalyst surfaces upon reduction can also be attained via a detailed analysis of the XPS data (Figures 4 and S2). Figure 4a,b presents the Mn 3s and O 1s XP spectra of the LMO catalyst as well as its reduced and spent forms. In addition, Figure 4c,d illustrates the B.E. splitting values of the Mn 3s signals and the average oxidation state of the surface Mn species, respectively. It is well known that although the most intense XPS signature of Mn is the Mn 3p signal (see Figure S2), this signal is not sufficiently sensitive to the oxidation state changes due to its convoluted nature. In contrast, despite its weaker XPS intensity, the Mn 3s signal can be much more informative about the surface oxidation state differences, allowing more precise estimation of the Mn surface oxidation states.<sup>40</sup> Particularly, the binding energy difference between the Mn 3s signal and its satellite (i.e.,  $\Delta\text{Mn } 3s$ ) can be exploited to estimate the average oxidation state (AOS) of surface Mn species using the following equation:  $\text{AOS} = 8.95 - 1.13 (\Delta\text{Mn } 3s)$ .<sup>40,41</sup> Figure 4d shows that the AOS of surface Mn species on the unreduced LMO catalyst is +3.6. This is in perfect agreement with the current XANES data (Figure S1), which also suggests that the average bulk oxidation state of  $\text{Mn}^{x+}$  B-site cations is  $+3 < x < +4$ . The influence of the reduction protocol on the surface Mn species on the LMO catalysts is also clearly visible in Figure 4d, where a gradual decrease in the surface Mn oxidation state (i.e., from +3.6 to +2.8) is discernible as a result of an increase in the reduction temperature to 1073 K. It should be noted that the best performing LMO-873K catalyst reveals a distinct surface Mn AOS of +3.1.

O 1s XPS data presented in Figure 4b is also particularly in good accordance with the current XRD (Figure 1a,b) and Mn 3s XPS (Figure 4a,c,d) data, revealing the gradual deformation of the perovskite structure and its eventual transformation to  $\text{La}_2\text{O}_3$  and MnO as a function of increasing reduction temperature. Figure 4b shows that the unreduced LMO catalyst has two major O 1s features located at 529.0 and 531.3 eV, which can be attributed to the perovskite structure and the residual surface oxygenates (such as  $-\text{CO}_x$  and  $-\text{C}_x\text{H}_y\text{O}_z$ ), respectively.<sup>40,42</sup> It is apparent that increasing reduction temperatures leads to broadening of the O 1s signals and the formation of a new high B.E. feature at ca. 531.7 eV due to decomposition of the perovskite structure into  $\text{La}_2\text{O}_3$  and MnO phases. Currently obtained La 3d XPS data (Figure S2a) is also consistent with the former studies in the literature on  $\text{LaMnO}_3$  systems and indicates the presence of  $\text{La}^{3+}$  surface states.<sup>43</sup> In line with the XPS data given in Figure 4b, reduction of the LMO at elevated temperatures also results in the broadening and deformation of the La 3d signals, suggesting drastic changes in the chemical environment of the  $\text{La}^{3+}$  ions.

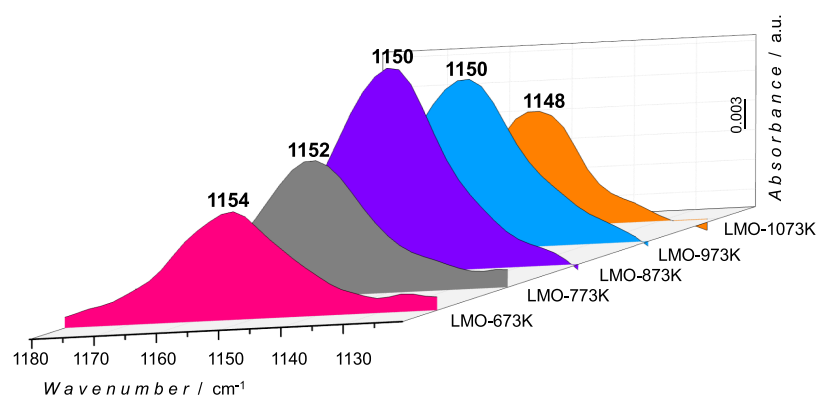


**Figure 5.** *In situ* FTIR spectra for low-temperature (150 K) O<sub>2</sub>(g) adsorption on reduced forms of LMO catalysts.

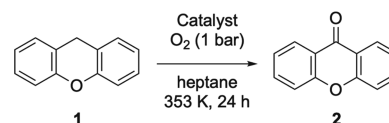
While the XPS technique is quite useful to elucidate the variations in the surface atomic composition and the oxidation states of surface species, it cannot provide unambiguous information about the relative concentration of oxygen vacancies that play a very significant role in the catalytic activity of perovskite catalysts. Therefore, to shed light on the oxygen vacancy formation on the LMO catalyst and its reduced forms, we performed *in situ* transmission Fourier transform infrared (*in situ* FTIR) spectroscopy experiments. Along these lines, we utilized O<sub>2</sub> as a probe molecule in the current *in situ* FTIR spectroscopic studies, where we investigated low-temperature (150 K) O<sub>2</sub>(g) adsorption on the perovskite catalysts. It is known that low-temperature adsorption of O<sub>2</sub> on reducible metal oxides may result in a unique vibrational signature around 1150 cm<sup>-1</sup>, which is due to the formation of metastable superoxide (O<sub>2</sub><sup>-</sup>(ads)) surface species.<sup>26</sup> Therefore, relative intensities of the O<sub>2</sub><sup>-</sup>(ads) vibrational features generated upon low-temperature O<sub>2</sub> adsorption can be exploited to compare relative surface oxygen vacancy concentrations on different reducible oxides. In light of this valuable information, *in situ* FTIR spectra shown in Figure 5 clearly suggest that increasing reduction temperature within 673–873 K monotonically increases the formation of surface oxygen vacancies on the reduced LMO surfaces. However, upon extreme reduction at 973 and 1073 K, decomposition of the perovskite structure results in the formation of La<sub>2</sub>O<sub>3</sub> and MnO phases with a lower total surface oxygen vacancy concentration than that of LMO-873K. This important experiment points to the fact that surface oxygen defect density of the LaMnO<sub>3+δ</sub> type perovskites can be fine-tuned by carefully chosen reduction protocols and the best performing LMO-873K catalyst has the highest relative surface oxygen vacancy concentration.

Comprehensive characterization results presented above unequivocally suggest that by careful utilizing currently presented synthetic protocols, one can modify the bulk crystal structure, specific surface area, surface atomic composition, and surface oxidation states of the catalytically active B-site cations as well as the surface concentration of oxygen vacancies on LaMnO<sub>3+δ</sub>-type perovskites with high precision. In light of these results, it is clear that the best performing catalyst (LMO-873K) has unique properties such a relatively disordered orthorhombic bulk crystal structure with multiple/heterogeneous surface domains, moderate SSA (14 m<sup>2</sup>/g), a high La/Mn surface atom ratio of 1.5, an average surface Mn oxidation state of +3.1, and the greatest capacity to generate adsorbed superoxide species, which can be linked to the presence of a large concentration of reactive surface oxygen vacancies on the

LMO-873K surface. As will be demonstrated in the next section, the ability to meticulously control the electronic, morphological, and surface chemical properties of LaMnO<sub>3+δ</sub>-type perovskites allowed us to obtain novel heterogeneous catalytic architectures with unusually high catalytic performance in C–H activation reactions involving alkylarene partial oxidation and naphthol dimerization.

**Catalytic Performance Tests.** We commenced our catalytic activity studies by examining the aerobic oxidation of 9*H*-xanthene (xanthene, **1**) to 9*H*-xanthen-9-one (xanthone, **2**) (Scheme 1). Initially, the reactions were run with a catalyst

**Scheme 1.** Aerobic oxidation of xanthene (**1**) to xanthone (**2**)



loading of 100 mg per 0.50 mmol substrate at 353 K in heptane. For the unreduced LMO catalyst, xanthone (**2**) was observed to form with 77% conversion, as determined by <sup>1</sup>H NMR spectroscopy (Figure 6). Modification of the perovskite catalyst with 4% H<sub>2</sub>(g) in Ar(g) at elevated temperatures was discovered to have a profound effect on the catalytic activity. Indeed, LMO

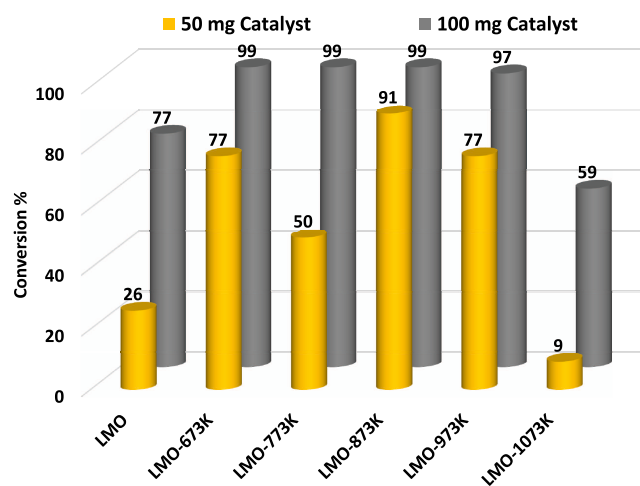


**Figure 6.** Catalytic activity of unreduced LMO catalyst and its reduced forms at 673–1073 K in aerobic oxidation of xanthene to xanthone (reaction conditions: P<sub>O<sub>2</sub></sub> = 1 bar, 0.50 mmol of xanthene at 353 K in heptane).

Table 1. Catalytic Aerobic Oxidation of Alkylarenes to Ketones\*

Entry	Substrate	Product	Conversion (%)	C-H BDE <sup>[d]</sup> (kcal/mol)
1 <sup>[a]</sup>			99 (97) <sup>[c]</sup>	80.7
2 <sup>[b]</sup>			99 (96) <sup>[c]</sup>	82.0
3 <sup>[a]</sup>			17	84.5

<sup>a</sup>0.50 mmol of substrate and 100 mg of catalyst were used. <sup>b</sup>0.50 mmol of substrate and 150 mg of catalyst were used. <sup>c</sup>Isolated product yield after purification by column chromatography is given in parentheses. <sup>d</sup>Homolytic bond dissociation (BDE) energies for the oxidized C–H bonds.

catalysts, which were subjected to the reductive pretreatment procedure at 673, 773, and 873 K, all afforded xanthone (**2**) product with almost full conversion (99%, Figure 6) within the first 24 h of the reaction. Whereas pretreatment at 973 K still provided an active catalyst (97% conversion), pretreatment at 1073 K gave a significantly inferior result (59%). It should be noted that xanthone product was obtained in 97% yield when the reaction mixture, where LMO-873K was used as the catalyst, was purified by column chromatography. This result points to a particularly good agreement between the isolated product yield (97%) and conversion value determined by <sup>1</sup>H NMR spectroscopy (99%). The conversion values for this reaction were determined after 3, 6, 9, and 24 h, and the results are summarized in Figure S3. It is clearly seen from these data that the reaction reaches 95% conversion at the end of 9 h. With these promising results in hand, we next examined the effect of catalyst amount on the reaction outcome. The results obtained with a catalyst loading of 50 mg per 0.50 mmol substrate are also shown in Figure 6. To our delight, the LaMnO<sub>3</sub> catalyst pretreated at 873 K retained almost all its catalytic activity at this catalyst loading, and xanthone (**2**) product was observed to form with 91% conversion within the first 24 h of the reaction. It should be noted that SrMnO<sub>3</sub> was used by Hara and co-workers in 2017 as a perovskite catalyst for aerobic oxidation reactions including the transformation of xanthene (**1**) to xanthone (**2**).<sup>27</sup> In this reaction, oxidation product **2** was obtained in 82% yield with the use of 100 mg of SrMnO<sub>3</sub> catalyst per 0.50 mmol substrate and 1 atm of O<sub>2</sub> at 353 K in 12 h. In addition, precious metal-catalyzed processes that have been reported in the literature for this oxidation reaction are known to operate under comparable reaction conditions with those reported in the current work. For instance, the use of Ir/TiO<sub>2</sub> catalyst (5 wt %) and molecular oxygen as the oxidant was reported to be effective for the catalytic oxidation of xanthene (**1**) to xanthone (**2**) with >99% conversion at 423 K with a reaction time of 12 h.<sup>44</sup> In another

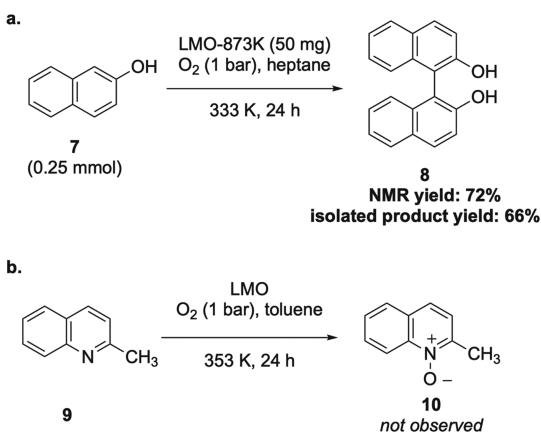
study, xanthone product (**2**) was obtained with >99% conversion and 92% isolated yield through the use of a Ru(OH)<sub>x</sub>/Al<sub>2</sub>O<sub>3</sub> catalyst (2 mol %) and molecular oxygen at 373 K in 2 h.<sup>45</sup>

After the successful completion of optimization studies, the utility of the catalytic C–H oxidation reaction was examined with other related substrates (Table 1). As aforementioned, xanthone (**2**) was obtained with almost full conversion (99%) with the use of molecular oxygen (P<sub>O<sub>2</sub></sub> = 1 bar) and LMO-873K catalyst (entry 1). Gratifyingly, 9H-fluorene (**3**) was observed to be a competent substrate under these oxidative conditions, and 9H-fluoren-9-one (fluorenone, **4**) was formed with 99% conversion (entry 2). When the product was purified by column chromatography, fluorenone (**4**) was isolated in 96% yield in a pure form. Finally, 1,1'-methylenebis(phenyl) (diphenylmethane, **5**) proved to be a less reactive substrate in this catalytic oxidation protocol as diphenylmethanone (benzophenone, **6**) was formed with only 17% conversion (entry 3). Overall, the reactivities of these three substrates (**1**, **3**, and **5**) were observed to be inversely proportional to the strengths of the corresponding C–H bonds as can be seen from their homolytic bond dissociation energies (Table 1).<sup>34,46–48</sup>

We next opted to test the effectiveness of the LMO-catalyzed aerobic oxidation process in mechanistically different oxidation reactions. Oxidative dimerization of 2-naphthols gives rise to the formation of 1,1'-binaphthyl-2,2'-diol (BINOL) derivatives, which are privileged ligands in enantioselective catalysis due to their axially chiral nature.<sup>49–51</sup> Moreover, BINOLs have gained considerable importance in the past two decades for being precursors of chiral phosphoric acid-type Brønsted acid catalysts.<sup>52–55</sup> Whereas oxidative dimerization of 2-naphthol (**7**) to BINOL (**8**) is well known,<sup>56</sup> the utilization of perovskites as heterogeneous catalysts in this process, to the best of our knowledge, has yet to be reported. Pleasingly, this transformation was observed to proceed efficiently when 2-naphthol

(7) was oxidized in the presence of O<sub>2</sub> in heptane at 333 K with the LMO-873K catalyst. Under these conditions, BINOL (8) was produced with a <sup>1</sup>H NMR yield of 72%, determined *via* the use of 1,3,5-trimethoxybenzene as an internal standard (Scheme 2a). Purification of the product by column chromatography

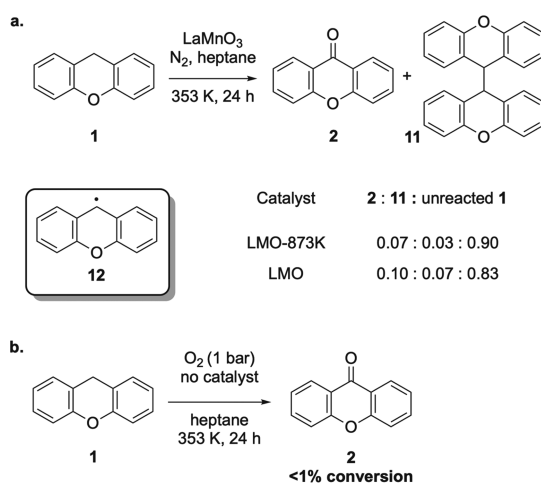
**Scheme 2. Studies on the Catalytic Oxidative Dimerization of 2-Naphthol (7) and Oxidation of 2-Methylquinoline (9)**



afforded BINOL (8) in 66% isolated product yield. Afterward, oxidation of azines to azine *N*-oxides, which are highly versatile building blocks in heterocyclic chemistry, was targeted.<sup>57,58</sup> For this purpose, we attempted the catalytic oxidation of 2-methylquinoline (quinaldine, 9) to 2-methylquinoline *N*-oxide (quinaldine *N*-oxide, 10) (Scheme 2b).<sup>59</sup> This latter transformation does not involve a C–H bond-breaking step and is expected to proceed *via* a direct oxygen atom transfer process. Unfortunately, the formation of the targeted *N*-oxide product 10 was not observed under the newly developed catalytic conditions.

**Mechanistic Studies.** To shed light on the mechanism of the LMO-catalyzed C–H oxidation reaction, we performed control experiments. First, the effect of the presence of oxygen was investigated. For this purpose, the oxidation of xanthene (1) was tested under the optimized reaction conditions in the absence of O<sub>2</sub>. In these experiments, the reaction mixtures were deoxygenated *via* the freeze–pump–thaw technique under an inert atmosphere of nitrogen. When a mixture of xanthene and LMO-873K in heptane was heated in the absence of O<sub>2</sub> at 353 K for 24 h, xanthone product 2 was observed to form with only 7% conversion along with 90% unreacted xanthene (1). In addition, the reaction gave rise to dimerization side product 9,9'-bixanthene (11) with 3% conversion (Scheme 3a).<sup>60–62</sup> It should be noted that this dimerization product 11 was not observed in catalytic oxidation reactions described in the previous section. When LMO was used under the same conditions, xanthone (2) and dimer 11 were observed to form in 10 and 7% conversions, respectively, along with 83% of unreacted xanthene (1). These results underscore the critical role of molecular oxygen in the oxidation reaction as the active oxidant. Moreover, formation of side product 11 gives an important clue regarding the reaction mechanism, as this product would form *via* the dimerization of the radical intermediate 12, which is expected to form by hydrogen atom abstraction from xanthene (1). In a separate control experiment, the oxidation of xanthene (1) was tested under the optimized reaction conditions but in the absence of a LaMnO<sub>3</sub> catalyst (Scheme 3b). In accordance with our expectations, the reaction

**Scheme 3. Effects of (a) O<sub>2</sub> and (b) Catalyst on the Reaction Outcome**



did not proceed under these conditions, and the formation of xanthone product 2 was not observed.

In light of our mechanistic and spectroscopic studies as well as the literature precedents, we propose the following mechanism for the LaMnO<sub>3</sub>-catalyzed C–H oxidation reaction (Figure 7). The activation of molecular oxygen on the surface of LaMnO<sub>3</sub> is proposed to produce surface-bound superoxide anions. *In situ* FTIR spectroscopic studies presented in the previous section not only support this step but also provide a correlation with the observed catalytic activity. Hydrogen atom abstraction from the benzylic position of xanthene (1) with a superoxide anion would produce the radical intermediate 12, which is relatively stabilized at the doubly benzylic position. When the LaMnO<sub>3</sub>-catalyzed oxidation reactions of xanthene (1), fluorene (3), and diphenylmethane (5) are compared, it can be concluded that the reactivity in the overall process increases with a decrease in the homolytic bond dissociation energy (BDE) of the corresponding C–H bond (Table 1). The rebound of the radical intermediate 12 with a hydroperoxide (HOO•) species is expected to result in the formation of intermediate 13. This intermediate can transform to xanthone (2) either directly *via* a dehydration reaction (path A) or through the intermediacy of the secondary alcohol intermediate 14 (path B). Finally, it should be noted that, in the absence of O<sub>2</sub>, radical intermediate 12 undergoes a radical homocoupling reaction to give 9,9'-bixanthene (11) as a side product.

**Studies on Catalyst Deactivation, Regeneration, and Reusability.** After the completion of structural characterization, catalytic performance, and mechanistic studies, we conducted reusability tests on the LMO-873K catalyst using the aerobic oxidation of xanthene to xanthone as the model reaction. This catalyst performed poorly (with 5% conversion of xanthene to xanthone) after it was centrifuged three times with ethyl acetate and finally taken with methanol into an evaporating dish for drying at 403 K prior to its second catalytic cycle. Fortunately, LMO-873K showed better catalytic activity with 63% conversion when it was subjected to regeneration *via* reduction at 873 K for 3 h under 100 sccm 4% H<sub>2</sub> in argon in a flow furnace. This regeneration procedure proved to be the best, among others. A similar regeneration method was applied by extending the reduction time from 3 to 6 h, but in this case, only 16% conversion was achieved. In a different approach, after calcination at 973 K, the catalyst was subjected to reduction at

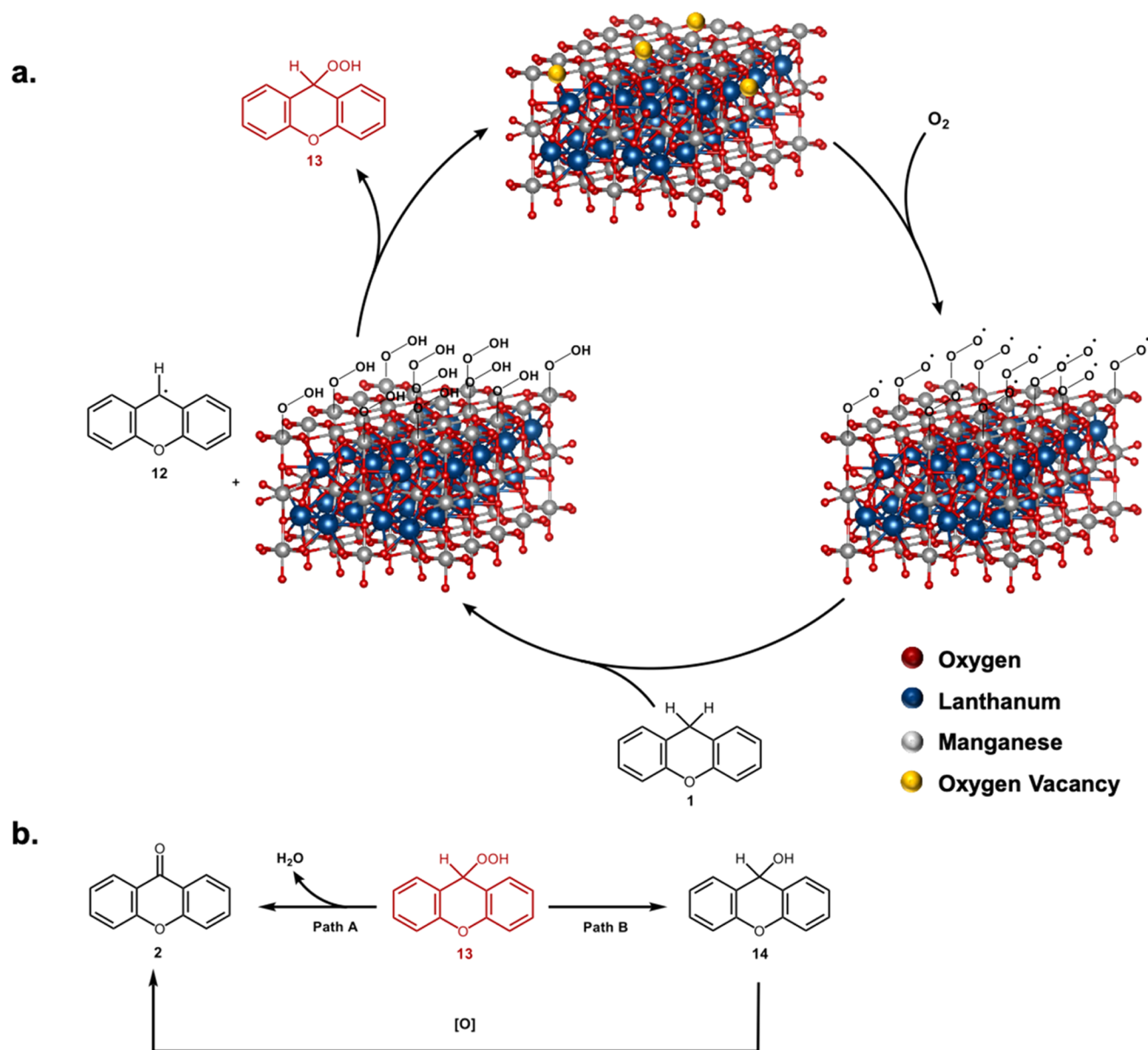


**Figure 7.** (a) Proposed mechanism for the aerobic oxidation of xanthene to xanthone catalyzed by LMO-873K. (b) Possible reaction pathways for the conversion of intermediate 13 to xanthone.

873 K for 3 h under 100 sccm 4% H<sub>2</sub> in argon in the flow furnace but yielded 18% conversion. The final regeneration method attempted included the introduction of the spent catalyst to ozone for 2 h at room temperature before reduction at 873 K for 3 h under 100 sccm 4% H<sub>2</sub> in argon in the flow furnace. Disappointingly, this method resulted in a low conversion of 7%. The details of the methods used for catalyst regeneration and the results obtained for each method are provided in Table S2 (Section S4 of the SI).

Currently performed detailed characterization experiments provide valuable information regarding the nature of the spent catalyst (i.e., LMO-873K\_Spent) and the molecular level origins of its catalytic deactivation routes. XPS surface elemental composition data given in Figure 3a clearly shows a significant amount of C accumulation and depletion of the O 1s signal on the LMO-873K catalyst surface after a typical reaction run (i.e., LMO-873K\_Spent catalyst in Figure 3a). Furthermore, Figure 3b indicates that the La/Mn surface atomic ratio of the LMO-

873K\_Spent catalyst is also lower than that of its fresh counterpart (i.e., LMO-873K). These observations suggest that the LMO-873K\_Spent catalyst surface is poisoned with reactants, products, or reaction intermediates. Also, surface compositional changes (i.e., excessive enrichment of the spent catalyst surface with La) could be another likely cause of catalytic deactivation. Note that the decrease in the surface O 1s signal in the spent catalyst as opposed to its fresh counterpart (Figure 3a) cannot be unambiguously associated with the changes in the surface oxygen vacancy content of the catalyst due to the presence of large amounts of -OH, -CO<sub>x</sub>, and -C<sub>x</sub>H<sub>y</sub>O<sub>z</sub> species on the catalyst surface. Furthermore, Mn 3s XPS data given in Figure 4d also point out to the fact that the average Mn surface oxidation state also changes from Mn<sup>+3.1</sup> (LMO-873K) to Mn<sup>+2.8</sup> (LMO-873K\_Spent) after the reaction, emphasizing alterations in the electronic structure of the catalytically active B-site cations upon deactivation. Similarly, significant broadening and changes in the spectral line shape of

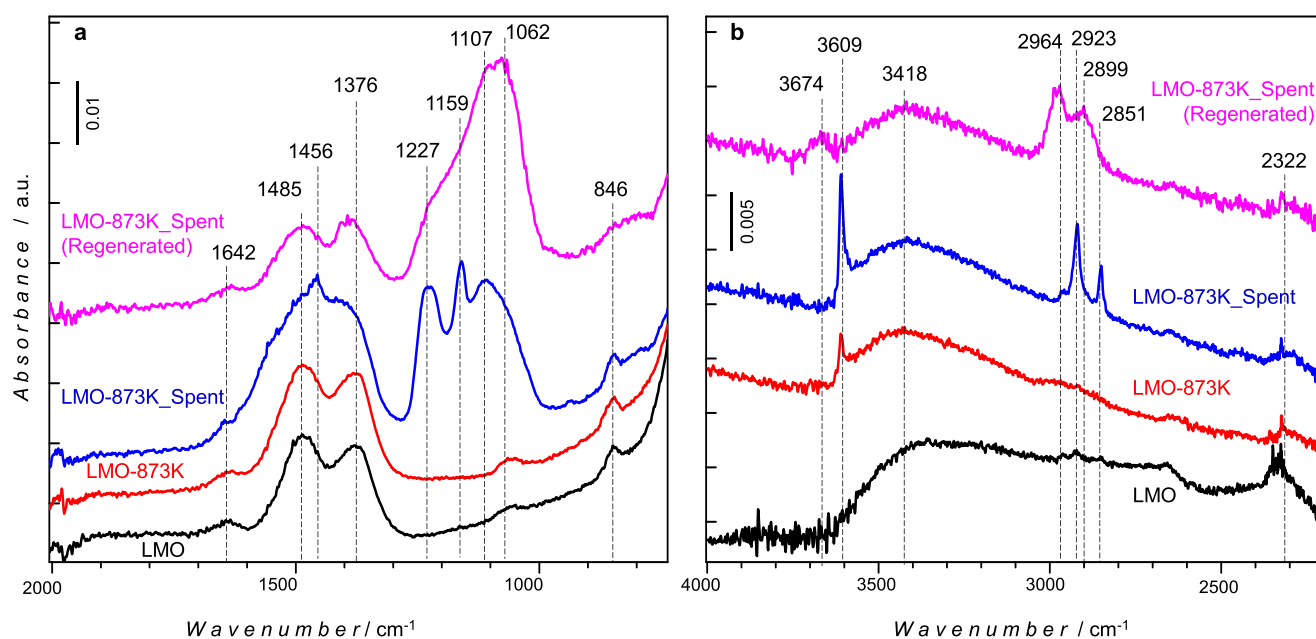


**Figure 8.** ATR-FTIR spectra of LMO, LMO-873K, LMO-873K-Spent, and LMO-873K\_Spent (regenerated) catalysts.

the O 1s XPS signal (Figure 4b) of LMO-873K after the catalytic reaction (LMO-873K\_Spent) are also consistent with the modification of the surface chemistry of the catalyst upon deactivation.

We also carried out detailed attenuated total reflection infrared (ATR-IR) spectroscopic analysis on the unreduced (LMO), reduced (i.e., LMO-873K), spent (LMO-873K\_Spent), and the regenerated form of LMO-873K to follow the functional group changes occurring on these surfaces (Figure 8a,b). Vibrational spectra in Figure 8 can be analyzed using conventional IR signatures of common organic functional groups.<sup>63,64</sup> It is apparent that the unreduced LMO catalyst (black spectra in Figure 8) reveals strong vibrational features within 1300–1550  $\text{cm}^{-1}$ , which can be attributed to the presence of surface carbonate species, in addition to weak features at 1062, 1642, and 2850–2960  $\text{cm}^{-1}$ , which can be assigned to  $\text{C}(\text{sp}^3)\text{-O}$  stretchings, adsorbed water (and/or  $\text{-C=C-}$  stretch) stretchings, and aliphatic  $\text{-CH}_x$  stretchings, respectively. The broad vibrational band centered at 3418  $\text{cm}^{-1}$  can be assigned to H-bonded  $\text{-OH}$  groups. Reduction of LMO at 873 K (LMO-873K, red spectra in Figure 8) leads to the formation of isolated  $\text{-OH}$  surface functionalities, as evident by the sharp IR signal at 3609  $\text{cm}^{-1}$ .

After the catalytic reaction, the LMO-873K\_Spent catalyst (blue spectra in Figure 2) revealed additional vibrational features, indicating the adsorption of various reactants, products, intermediates, and the solvent. As a result, multiple convoluted IR bands in the corresponding spectra within 1000–1300  $\text{cm}^{-1}$  can be ascribed to  $\text{-C}(\text{sp}^3)\text{-O}$  (1000–1100  $\text{cm}^{-1}$ ) and  $\text{-C}(\text{sp}^2)\text{-O}$  (1200–1300  $\text{cm}^{-1}$ ) stretchings. On the spent catalyst, while the 1300–1550  $\text{cm}^{-1}$  features can be attributed to the carbonate features, the remaining feature at 1456  $\text{cm}^{-1}$  can be assigned to  $\text{-CH}$  or  $\text{-CH}_2$  bending modes. Furthermore, the intensities of the aliphatic  $\text{-CH}_x$  stretchings within 2850–2960  $\text{cm}^{-1}$  and the isolated  $\text{-OH}$  stretchings at 3609  $\text{cm}^{-1}$  were found to increase noticeably on the LMO-873K\_Spent catalyst.

As mentioned above, the currently used regeneration protocol did not allow us to fully recover the initial activity and enabled only partial regeneration of the spent catalyst. This behavior was

also consistent with the corresponding ATR-IR spectrum of the regenerated catalyst. ATR-IR spectra of the regenerated LMO-873K\_Spent catalyst (purple spectra in Figure 8) show that vibrational signatures within 1300–1550  $\text{cm}^{-1}$  are mostly recovered with an increase in the  $\text{-C}(\text{sp}^3)\text{-O}$  (1000–1100  $\text{cm}^{-1}$ ) and aliphatic  $\text{-CH}_x$  (2850–2960  $\text{cm}^{-1}$ ) stretchings, where the latter features also reveal a blue shift in frequency. Also, after the regeneration, isolated  $\text{-OH}$  features at 3609  $\text{cm}^{-1}$  completely vanished and a different weak  $\text{-OH}$  stretching signal became apparent at 3674  $\text{cm}^{-1}$ .

## CONCLUSIONS

In summary, we have developed a highly effective method for C–H oxidation reactions catalyzed by a  $\text{LaMnO}_3$ -based perovskite catalyst. This method does not involve the use of precious transition metals and utilizes molecular oxygen as the stoichiometric oxidant. Careful optimization of the catalyst revealed that a reductive pretreatment by 4%  $\text{H}_2$  in argon at 873 K afforded the  $\text{LaMnO}_3$  catalyst with the highest catalytic activity. The structural and electronic changes that arise as a result of this pretreatment protocol have been investigated in detail *via* a series of spectroscopic, microscopic, and diffraction studies. Alkylarene substrates xanthene and fluorene were shown to be oxidized to their corresponding ketone products xanthone and fluorenone in high yields (97 and 96%, respectively) with the use of the LMO-873K perovskite catalyst and molecular oxygen at 1 bar. In light of our detailed spectroscopic and mechanistic studies, a mechanism that involves the formation of a superoxide ( $\text{O}_2^-$ ) species on the catalyst surface and subsequent H-atom abstraction from the C–H group was proposed for the alkylarene oxidation. Moreover, the current catalytic method proved to be effective for the synthesis of 1,1'-binaphthyl-2,2'-diol (BINOL) *via* the oxidative aerobic dimerization of 2-naphthol. Catalytic performance and the spectroscopic experiments revealed that, upon extensive use, catalysts were deactivated due to the adsorption of reactants/products/intermediates as well as surface chemical alterations on the catalyst. It was demonstrated that deactivated

perovskite catalysts can be reactivated to a certain extent using a variety of regeneration protocols.

## EXPERIMENTAL SECTION

**Chemicals and Catalyst Preparation.**  $\text{La}(\text{NO}_3)_3 \cdot 6\text{H}_2\text{O}$ ,  $\text{Mn}(\text{NO}_3)_3$ , and citric acid were purchased from Millipore Sigma and used as received. The citrate method was employed in the synthesis of  $\text{LaMnO}_3$ .<sup>65</sup>  $\text{La}(\text{NO}_3)_3 \cdot 6\text{H}_2\text{O}$  (5.372 g),  $\text{Mn}(\text{NO}_3)_3$  (3.114 g), and citric acid (5.735 g) were dissolved in 250 mL of deionized water and stirred at room temperature for 1 h. Then, the mixture was heated at 353 K until the formation of a viscous gel concomitant with the evolution of a brown gas (i.e.,  $\text{NO}_2$ ). The obtained gel was dried in an oven at 383 K for 24 h. The dried sample was ground to its powdered form and calcined at 973 K for 5 h. The LMO acronym used in the text corresponds to this particular state of the  $\text{LaMnO}_3$  catalyst. Reduced LMO catalysts were prepared *via* reducing LMO catalyst under 100 sccm 4%  $\text{H}_2$  in Ar for 3 h at 673, 773, 873, 973, and 1073 K in a flow furnace.

**Instrumentation.** A Rigaku diffractometer, equipped with a Miniflex goniometer and an X-ray source with Cu  $K\alpha$  radiation at  $\lambda = 1.5418 \text{ \AA}$ , 30 kV, and 15 mA, was used to record the powder X-ray diffraction (XRD) patterns at a scan rate of  $0.02^\circ \text{ s}^{-1}$  in the  $10\text{--}80^\circ 2\theta$  range. Diffraction patterns were assigned using PDF cards from the International Centre for Diffraction Database (ICDD).

A Micromeritics Tristar 3000 surface area and pore size analyzer was used to measure the BET specific surface area values by low-temperature isothermal adsorption–desorption of  $\text{N}_2$ . All samples were initially outgassed at 573 K for 2 h in vacuum prior to BET measurements.

X-ray photoelectron spectroscopy (XPS) measurements were performed using a SPECS XPS system equipped with an X-ray source (Al/Ag dual anode), an ellipsoidal crystal Al  $K\alpha$  X-ray monochromator, a FOCUS-500 excitation source (15 kV, 400 W), and a PHOIBOS 150 hemispherical electron energy analyzer. Binding energy values of the XP spectra were calibrated using the adventitious carbon (C 1s) signal located at 284.5 eV.

*In situ* transmission Fourier transform infrared (FTIR) spectroscopic measurements were carried out in a batch-type catalytic reactor coupled to an FTIR spectrometer (Bruker Tensor 27) equipped with a Hg–Cd–Te (MCT) detector. About 25 mg of finely ground LMO was pressed onto a high transmittance, lithographically etched fine-tungsten grid, which was mounted on a copper sample holder assembly. Prior to data acquisition, the *in situ* reactor chamber was evacuated to  $5 \times 10^{-6}$  Torr. Next, 5 Torr 5%  $\text{H}_2/\text{Ar}$  was dosed over the sample at room temperature (RT), then heated to 673 K, and held for 10 min in the presence of the  $\text{H}_2/\text{Ar}$  gas mixture. After the reduction protocol, the sample was cooled to RT, where the gas mixture was evacuated to  $5 \times 10^{-6}$  Torr. At this stage, the sample was cooled to 142 K by recirculating liquid nitrogen around the sample holder. After having taken a background FTIR spectrum at 142 K in vacuum, 1 Torr  $\text{O}_2$  was dosed over the sample for 1 min followed by subsequent evacuation for 1 min and sample spectrum acquisition. After the sample spectrum acquisition, the sample was brought back to RT. Then, by utilizing the same background spectrum, the steps described above were repeated by altering the reduction temperature to 773, 873, 973, and 1073 K. *In situ* FTIR spectra were recorded with a resolution of  $2 \text{ cm}^{-1}$  and by averaging 64 scans per spectrum.

ATR-FTIR spectra were acquired by using a Bruker Alpha Platinum FTIR spectrometer equipped with a diamond ATR crystal module and a deuterated triglycine sulfate (DTGS) mid-IR detector. ATR-FTIR spectra were recorded at a resolution of  $2 \text{ cm}^{-1}$  and 128 scans per spectrum.

TEM measurements were performed in bright-field mode using an FEI Tecnai G2 F30 microscope with a specified point resolution of 0.17 nm and a Gatan slow-scan CCD camera. The operating voltage of the microscope was 300 keV during TEM imaging.

Reactions were monitored by thin-layer chromatography (TLC) using aluminum-backed plates precoated with  $\text{SiO}_2$  (Silicycle, F254). UV light (254 nm) was used for TLC visualization. Flash column

chromatography was performed using Silicycle 40–63  $\mu\text{m}$  (230–400 mesh) flash silica gel. NMR spectra were recorded on a Bruker spectrometer at 400 MHz for  $^1\text{H}$  NMR spectra and 100 MHz for  $^{13}\text{C}$  NMR spectra. They were calibrated *via* an internal standard (TMS, 0 ppm) or residual solvent signal (chloroform; at 7.26 ppm for  $^1\text{H}$  NMR spectra and at 77.16 ppm for  $^{13}\text{C}$  NMR spectra). High-resolution mass spectrometry (HRMS) analyses were performed at UNAM—National Nanotechnology Research Center and Institute of Materials Science and Nanotechnology, Bilkent University.

**9H-Xanthen-9-one (2).** A 25 mL Schlenk flask was charged with  $\text{LaMnO}_3$  (100 mg, pretreated at 873 K), xanthene (1) (90.4 mg, 0.50 mmol), and 2.0 mL of heptane. The flask was filled with  $\text{O}_2$  gas (1 bar) and sealed. The reaction mixture was stirred at 353 K in an oil bath for 24 h. It was then cooled to ambient temperature, diluted with EtOAc, and passed through Celite. Purification by flash column chromatography ( $\text{SiO}_2$ , EtOAc/hexane = 1:3) gave pure xanthone (2) (95.1 mg, 97% yield) as a white solid.  $^1\text{H}$  NMR (400 MHz,  $\text{CDCl}_3$ )  $\delta$  8.35 (2H, dd,  $J = 7.8, 1.5 \text{ Hz}$ ), 7.73 (2H, ddd,  $J = 8.8, 7.1, 1.7 \text{ Hz}$ ), 7.50 (2H, dd,  $J = 8.5, 0.7 \text{ Hz}$ ), 7.38 (2H, ddd,  $J = 8.1, 7.1, 1.0 \text{ Hz}$ ).  $^{13}\text{C}$  NMR (100 MHz,  $\text{CDCl}_3$ )  $\delta$  177.4, 156.3, 135.0, 126.9, 124.1, 122.0, 118.1. HRMS (APCI+) calcd for  $(\text{C}_{13}\text{H}_9\text{O}_2)^+$  ( $M + H$ ): 197.0598, found: 197.0607. The spectral data are in agreement with the reported values in the literature.<sup>66</sup>

**9H-Fluoren-9-one (4).** A 25 mL Schlenk flask was charged with  $\text{LaMnO}_3$  (150 mg, pretreated at 873 K), fluorene (3) (83.1 mg, 0.50 mmol), and 2.0 mL of heptane. The flask was filled with  $\text{O}_2$  gas (1 bar) and sealed. The reaction mixture was stirred at 353 K in an oil bath for 24 h. It was then cooled to ambient temperature, diluted with EtOAc, and passed through Celite. Purification by flash column chromatography ( $\text{SiO}_2$ , gradual increase of polarity from hexane to 30% EtOAc in hexane) gave pure fluorenone (4) (86.9 mg, 96% yield) as a yellow solid.  $^1\text{H}$  NMR (400 MHz,  $\text{CDCl}_3$ )  $\delta$  7.66 (2H, d,  $J = 7.6 \text{ Hz}$ ), 7.53 (2H, d,  $J = 7.3 \text{ Hz}$ ), 7.49 (2H, dt,  $J = 7.4, 1.2 \text{ Hz}$ ), 7.30 (2H, dt,  $J = 7.3, 1.2 \text{ Hz}$ ).  $^{13}\text{C}$  NMR (100 MHz,  $\text{CDCl}_3$ )  $\delta$  194.0, 144.6, 134.8, 134.3, 129.2, 124.4, 120.4. HRMS (APCI+) calcd for  $(\text{C}_{13}\text{H}_9\text{O})^+$  ( $M + H$ ): 181.0648, found: 181.0657. The spectral data are in agreement with the reported values in the literature.<sup>67</sup>

**1,1'-Binaphthyl-2,2'-diol (BINOL) (8).** A 25 mL Schlenk flask was charged with  $\text{LaMnO}_3$  (50 mg, pretreated at 873 K), 2-naphthol (7) (36.0 mg, 0.25 mmol), and 1.0 mL of heptane. The flask was filled with  $\text{O}_2$  gas (1 bar) and sealed. The reaction mixture was stirred at 333 K in an oil bath for 24 h. It was then cooled to ambient temperature, diluted with EtOAc, and passed through Celite. Purification by flash column chromatography ( $\text{SiO}_2$ , first chromatography with EtOAc/hexane = 1:9; second chromatography with EtOAc/hexane = 1:4) gave pure BINOL (8) (23.6 mg, 66% yield) as a red solid.  $^1\text{H}$  NMR (400 MHz,  $\text{CDCl}_3$ )  $\delta$  7.97 (2H, d,  $J = 8.9 \text{ Hz}$ ), 7.89 (2H, d,  $J = 8.0 \text{ Hz}$ ), 7.39–7.37 (4H, m), 7.30 (2H, t,  $J = 7.6 \text{ Hz}$ ), 7.15 (2H, d,  $J = 8.4 \text{ Hz}$ ), 5.05 (2H, s).  $^{13}\text{C}$  NMR (100 MHz,  $\text{CDCl}_3$ )  $\delta$  152.9, 133.6, 131.6, 129.6, 128.6, 127.6, 124.4, 124.2, 117.9, 111.0. HRMS (APCI–) calcd for  $(\text{C}_{20}\text{H}_{13}\text{O}_2)^-$  ( $M - H$ ): 285.0921, found: 285.0929. The spectral data are in agreement with the reported values in the literature.<sup>68</sup>

**9,9'-Bixanthen (11).**  $^1\text{H}$  NMR (400 MHz,  $\text{CDCl}_3$ )  $\delta$  7.20 (4H, dt,  $J = 8.2, 1.6 \text{ Hz}$ ), 6.93 (4H, dt,  $J = 7.5, 1.1 \text{ Hz}$ ), 6.87 (2H, dd,  $J = 8.1, 0.9 \text{ Hz}$ ), 6.66 (4H, dd,  $J = 7.6, 1.5 \text{ Hz}$ ), 4.20 (2H, s).  $^{13}\text{C}$  NMR (100 MHz,  $\text{CDCl}_3$ )  $\delta$  153.2, 129.3, 128.3, 122.8, 122.0, 116.0, 49.7. The spectral data are in agreement with the reported values in the literature.<sup>61</sup>

## ASSOCIATED CONTENT

### Supporting Information

The Supporting Information is available free of charge at <https://pubs.acs.org/doi/10.1021/acsami.0c20490>.

Details of EXAFS and XANES experiments, additional XPS data, conversion data at different reaction times, details of studies on catalyst regeneration, and  $^1\text{H}$  and  $^{13}\text{C}$  NMR spectra (PDF)

## AUTHOR INFORMATION

## Corresponding Authors

Emrah Ozensoy – Department of Chemistry, Faculty of Science, Bilkent University, 06800 Ankara, Turkey; [orcid.org/0000-0003-4352-3824](https://orcid.org/0000-0003-4352-3824); Email: [ozensoy@fen.bilkent.edu.tr](mailto:ozensoy@fen.bilkent.edu.tr)

Yunus E. Türkmen – Department of Chemistry, Faculty of Science, Bilkent University, 06800 Ankara, Turkey; [orcid.org/0000-0002-9797-2820](https://orcid.org/0000-0002-9797-2820); Email: [yeturkmen@bilkent.edu.tr](mailto:yeturkmen@bilkent.edu.tr)

## Authors

Yesim Sahin – Department of Chemistry, Faculty of Science, Bilkent University, 06800 Ankara, Turkey

Abel T. Sika-Nartey – Department of Chemistry, Faculty of Science, Bilkent University, 06800 Ankara, Turkey

Kerem E. Ercan – Department of Chemistry, Faculty of Science, Bilkent University, 06800 Ankara, Turkey; [orcid.org/0000-0003-4650-7977](https://orcid.org/0000-0003-4650-7977)

Yusuf Kocak – Department of Chemistry, Faculty of Science, Bilkent University, 06800 Ankara, Turkey; [orcid.org/0000-0003-4511-1321](https://orcid.org/0000-0003-4511-1321)

Sinem Senol – Department of Chemistry, Faculty of Science, Bilkent University, 06800 Ankara, Turkey

Complete contact information is available at: <https://pubs.acs.org/10.1021/acsami.0c20490>

## Notes

The authors declare no competing financial interest.

## ACKNOWLEDGMENTS

Y.E.T. acknowledges the BAGEP Award of the Science Academy, Turkey. E.O. acknowledges the scientific collaboration with the TARLA project founded by the Ministry of Development of Turkey (project code DPT2006K–120470). E.O. and K.E.E. acknowledge the Turkish Atomic Authority (TAEK) for funding their travel to support X-ray absorption spectroscopy (XAS) studies. E.O. and K.E.E. also thank DESY and P65 beamline staff Dr. Edmund Welter and Dr. Roman Chernikov for their support in conducting XAS experiments. K.E.E. and Y.S. also acknowledge the COST (European Cooperation in Science and Technology) action CHAOS-CA15106 (C–H Activation in Organic Synthesis) for funding their travel within the scope of COST ITC Conference Grants.

## REFERENCES

- (1) Gandeepan, P.; Müller, T.; Zell, D.; Cera, G.; Warratz, S.; Ackermann, L. 3d Transition Metals for C–H Activation. *Chem. Rev.* **2019**, *119*, 2192–2452.
- (2) Chu, J. C. K.; Rovis, T. Complementary Strategies for Directed C(sp<sup>3</sup>)-H Functionalization: A Comparison of Transition-Metal-Catalyzed Activation, Hydrogen Atom Transfer, and Carbene/Nitrene Transfer. *Angew. Chem., Int. Ed.* **2018**, *57*, 62–101.
- (3) Sauermann, N.; Meyer, T. H.; Qiu, Y.; Ackermann, L. Electrocatalytic C–H Activation. *ACS Catal.* **2018**, *8*, 7086–7103.
- (4) He, J.; Wasa, M.; Chan, K. S. L.; Shao, Q.; Yu, J.-Q. Palladium-Catalyzed Transformations of Alkyl C–H Bonds. *Chem. Rev.* **2017**, *117*, 8754–8786.
- (5) Santoro, S.; Kozhushkov, S. I.; Ackermann, L.; Vaccaro, L. Heterogeneous Catalytic Approaches in C–H Activation Reactions. *Green Chem.* **2016**, *18*, 3471–3493.
- (6) Djakovitch, L.; Felpin, F.-X. Direct C sp<sup>2</sup>-H and C sp<sup>3</sup>-H Arylation Enabled by Heterogeneous Palladium Catalysts. *ChemCatChem* **2014**, *6*, 2175–2187.

(7) Wencel-Delord, J.; Glorius, F. C–H Bond Activation Enables the Rapid Construction and Late-Stage Diversification of Functional Molecules. *Nat. Chem.* **2013**, *5*, 369–375.

(8) Kal, S.; Xu, S.; Que, L., Jr. Bio-inspired Nonheme Iron Oxidation Catalysis: Involvement of Oxoiron(V) Oxidants in Cleaving Strong C–H Bonds. *Angew. Chem., Int. Ed.* **2020**, *59*, 7332–7349.

(9) Fessner, N. D. P450 Monooxygenases Enable Rapid Late-Stage Diversification of Natural Products via C–H Bond Activation. *ChemCatChem* **2019**, *11*, 2226–2242.

(10) Wang, V. C.-C.; Maji, S.; Chen, P. P.-Y.; Lee, H. K.; Yu, S. S.-F.; Chan, S. I. Alkane Oxidation: Methane Monooxygenases, Related Enzymes, and Their Biomimetics. *Chem. Rev.* **2017**, *117*, 8574–8621.

(11) Newhouse, T.; Baran, P. S. If C–H Bonds Could Talk: Selective C–H Bond Oxidation. *Angew. Chem., Int. Ed.* **2011**, *50*, 3362–3374.

(12) Luo, L.; Zhang, T.; Wang, M.; Yun, R.; Xiang, X. Recent Advances in Heterogeneous Photo-Driven Oxidation of Organic Molecules by Reactive Oxygen Species. *ChemSusChem* **2020**, *13*, 5173–5184.

(13) Larson, V. A.; Battistella, B.; Ray, K.; Lehnert, N.; Nam, W. Iron and Manganese Oxo Complexes, Oxo Wall and Beyond. *Nat. Rev. Chem.* **2020**, *4*, 404–419.

(14) Ottenbacher, R. V.; Talsi, E. P.; Bryliakov, K. P. Recent Progress in Catalytic Oxygenation of Aromatic C–H Groups with the Environmentally Benign Oxidants H<sub>2</sub>O<sub>2</sub> and O<sub>2</sub>. *Appl. Organomet. Chem.* **2020**, *34*, No. e5900.

(15) Cano, R.; Mackey, K.; McGlacken, G. P. Recent Advances in Manganese-Catalyzed C–H Activation: Scope and Mechanism. *Catal. Sci. Technol.* **2018**, *8*, 1251–1266.

(16) Roduner, E.; Kaim, W.; Sarkar, B.; Urlacher, V. B.; Pleiss, J.; Gläser, R.; Einicke, W.-D.; Sprenger, G. A.; Beifuß, U.; Klemm, E.; Liebner, C.; Hieronymus, H.; Hsu, S.-F.; Plietker, B.; Laschat, S. Selective Catalytic Oxidation of C–H Bonds with Molecular Oxygen. *ChemCatChem* **2013**, *5*, 82–112.

(17) Punniyamurthy, T.; Velusamy, S.; Iqbal, J. Recent Advances in Transition Metal Catalyzed Oxidation of Organic Substrates with Molecular Oxygen. *Chem. Rev.* **2005**, *105*, 2329–2363.

(18) Atta, N. F.; Galal, A.; El-Ads, E. H. *Perovskite Nanomaterials—Synthesis, Characterization, and Applications*; Pan, L.; Zhu, G., Eds.; IntechOpen, 2016; Vol. 1, pp 107–151.

(19) Royer, S.; Duprez, D.; Can, F.; Courtois, X.; Batiot-Dupeyrat, C.; Laassiri, S.; Alamdari, H. Perovskites as Substitutes of Noble Metals for Heterogeneous Catalysis: Dream or Reality. *Chem. Rev.* **2014**, *114*, 10292–10368.

(20) Peña, M. A.; Fierro, J. L. G. Chemical Structures and Performance of Perovskite Oxides. *Chem. Rev.* **2001**, *101*, 1981–2017.

(21) Zhu, H.; Zhang, P.; Dai, S. Recent Advances of Lanthanum-Based Perovskite Oxides for Catalysis. *ACS Catal.* **2015**, *5*, 6370–6385.

(22) Luo, D.; Su, R.; Zhang, W.; Gong, Q.; Zhu, R. Minimizing Non-Radiative Recombination Losses in Perovskite Solar Cells. *Nat. Rev. Mater.* **2020**, *5*, 44–60.

(23) Jin, S.; Tiffel, T. H.; McCormack, M.; Fastnacht, R. A.; Ramesh, R.; Chen, L. H. Thousandfold Change in Resistivity in Magnetoresistive La–Ca–Mn–O Films. *Science* **1994**, *264*, 413–415.

(24) Hu, Y.; Zhao, G.; Pan, Q.; Wang, H.; Shen, Z.; Peng, B.; Busser, G. W.; Wang, X.; Muhler, M. Highly Selective Anaerobic Oxidation of Alcohols Over Fe-doped SrTiO<sub>3</sub> Under Visible Light. *ChemCatChem* **2019**, *11*, 5139–5144.

(25) Mizuno, N. Ed. *Modern Heterogeneous Oxidation Catalysis*; Wiley-VCH: Weinheim, 2009.

(26) Kawasaki, S.; Kamata, K.; Hara, M. Dioxygen Activation by a Hexagonal SrMnO<sub>3</sub> Perovskite Catalyst for Aerobic Liquid-Phase Oxidation. *ChemCatChem* **2016**, *8*, 3247–3253.

(27) Sugahara, K.; Kamata, K.; Muratsugu, S.; Hara, M. Amino Acid-Aided Synthesis of a Hexagonal SrMnO<sub>3</sub> Nanoperovskite Catalyst for Aerobic Oxidation. *ACS Omega* **2017**, *2*, 1608–1616.

(28) Shibata, S.; Sugahara, K.; Kamata, K.; Hara, M. Liquid-Phase Oxidation of Alkanes with Molecular Oxygen Catalyzed by High Valent Iron-Based Perovskite. *Chem. Commun.* **2018**, *54*, 6772–6775.

- (29) Kamata, K.; Sugahara, K.; Kato, Y.; Muratsugu, S.; Kumagai, Y.; Oba, F.; Hara, M. Heterogeneously Catalyzed Aerobic Oxidation of Sulfides with a BaRuO<sub>3</sub> Nanoperovskite. *ACS Appl. Mater. Interfaces* **2018**, *10*, 23792–23801.
- (30) Zhu, X.; Lin, Y.; San Martin, J.; Sun, Y.; Zhu, D.; Yan, Y. Lead Halide Perovskites for Photocatalytic Organic Synthesis. *Nat. Commun.* **2019**, *10*, No. 2843.
- (31) Zhu, X.; Lin, Y.; Sun, Y.; Beard, M. C.; Yan, Y. Lead-Halide Perovskites for Photocatalytic  $\alpha$ -Alkylation of Aldehydes. *J. Am. Chem. Soc.* **2019**, *141*, 733–738.
- (32) Guo, Z.; Liu, B.; Zhang, Q.; Deng, W.; Wang, Y.; Yang, Y. Recent Advances in Heterogeneous Selective Oxidation Catalysis for Sustainable Chemistry. *Chem. Soc. Rev.* **2014**, *43*, 3480–3524.
- (33) For a review on C-H functionalization reactions of diaryl-methanes, see: Gulati, U.; Gandhi, R.; Laha, J. K. Benzylic Methylene Functionalizations of Diarylmethanes. *Chem. Asian J.* **2020**, *15*, 3135–3161.
- (34) Luo, Y.-R. *Handbook of Bond Dissociation Energies in Organic Compounds*; CRC Press: Boca Raton, 2003.
- (35) Kim, C. H.; Qi, G.; Dahlberg, K.; Li, W. Strontium-Doped Perovskites Rival Platinum Catalysts for Treating NO<sub>x</sub> in Simulated Diesel Exhaust. *Science* **2010**, *327*, 1624–1627.
- (36) Chen, J.; Shen, M.; Wang, X.; Qi, G.; Wang, J.; Li, W. The Influence of Nonstoichiometry on LaMnO<sub>3</sub> Perovskite for Catalytic NO Oxidation. *Appl. Catal., B* **2013**, *134–135*, 251–257.
- (37) Zhu, X.; Li, K.; Neal, L.; Li, F. Perovskites as Geo-inspired Oxygen Storage Materials for Chemical Looping and Three-Way Catalysis: A Perspective. *ACS Catal.* **2018**, *8*, 8213–8236.
- (38) Van Roosmalen, J. A. M.; Cordfunke, E. H. P. The Defect Chemistry of LaMnO<sub>3±δ</sub>: 4. Defect Model for LaMnO<sub>3±δ</sub>. *J. Solid State Chem.* **1994**, *110*, 109–112.
- (39) Subías, G.; Garcia, J.; Blasco, J.; Proietti, M. G. Effect of Cation Vacancies in the Local Structure and Transport Properties of LaMnO<sub>3±δ</sub>: A Mn K-edge X-Ray-Absorption Study. *Phys. Rev. B* **1998**, *58*, 9287–9293.
- (40) Nakai, S.; Uematsu, T.; Ogasawara, Y.; Suzuki, K.; Yamaguchi, K.; Mizuno, N. Aerobic Oxygenation of Alkylarenes over Ultrafine Transition-Metal-Containing Manganese-Based Oxides. *ChemCatChem* **2018**, *10*, 1096–1106.
- (41) Galakhov, V. R.; Demeter, M.; Bartkowski, S.; Neumann, M.; Ovechkina, N. A.; Kurmaev, E.; Lobachevskaya, N. I.; Mukovskii, Y. M.; Mitchell, J.; Ederer, D. L. Mn 3s Exchange Splitting in Mixed-Valence Manganites. *Phys. Rev. B* **2002**, *65*, No. 113102.
- (42) Mickevicius, S.; Grebinskij, S.; Bondarenka, V.; Vengalis, B.; Sluizene, K.; Orlovski, B. A.; Osinniy, V.; Drube, W. Investigation of Epitaxial LaNiO<sub>3-x</sub> Thin Films by High-Energy XPS. *J. Alloys Compd.* **2006**, *423*, 107–111.
- (43) Vasquez, R. P. X-Ray Photoemission Measurements of La<sub>1-x</sub>Ca<sub>x</sub>CoO<sub>3</sub> (x = 0, 0.5). *Phys. Rev. B* **1996**, *54*, 14938–14941.
- (44) Yoshida, A.; Takahashi, Y.; Ikeda, T.; Azemoto, K.; Naito, S. Catalytic Oxidation of Aromatic Alcohols and Alkylarenes with Molecular Oxygen over Ir/TiO<sub>2</sub>. *Catal. Today* **2011**, *164*, 332–335.
- (45) Kamata, K.; Kasai, J.; Yamaguchi, K.; Mizuno, N. Efficient Heterogeneous Oxidation of Alkylarenes with Molecular Oxygen. *Org. Lett.* **2004**, *6*, 3577–3580.
- (46) Rüchardt, C.; Gerst, M.; Ebenhoch, J. Uncatalyzed Transfer Hydrogenation and Transfer Hydrogenolysis: Two Novel Types of Hydrogen-Transfer Reactions. *Angew. Chem., Int. Ed.* **1997**, *36*, 1406–1430.
- (47) Rakus, K.; Verevkin, S. P.; Schätzer, J.; Beckhaus, H.-D.; Rüchardt, C. Thermochemistry and Thermal Decomposition of 9,9'-Bifluorenyl and 9,9'-Dimethyl-9,9'-bifluorenyl - The Stabilization Energy of 9-Fluorenyl Radicals. *Chem. Ber.* **1994**, *127*, 1095–1103.
- (48) Parker, V. D.; Handoo, K. L.; Roness, F.; Tilset, M. Electrode Potentials and the Thermodynamics of Isodesmic Reactions. *J. Am. Chem. Soc.* **1991**, *113*, 7493–7498.
- (49) Shibasaki, M.; Matsunaga, S. Design and Application of Linked-BINOL Chiral Ligands in Bifunctional Asymmetric Catalysis. *Chem. Soc. Rev.* **2006**, *35*, 269–279.
- (50) Brunel, J. M. BINOL: A Versatile Chiral Reagent. *Chem. Rev.* **2005**, *105*, 857–897.
- (51) Chen, Y.; Yekta, S.; Yudin, A. K. Modified BINOL Ligands in Asymmetric Catalysis. *Chem. Rev.* **2003**, *103*, 3155–3211.
- (52) Tay, J.-H.; Nagorny, P. Phosphoric Acid Catalysis. In *Nonnitrogenous Organocatalysis*; Harned, A. M., Ed.; CRC Press, Taylor & Francis: Boca Raton, 2018; pp 39–68.
- (53) Parmar, D.; Sugiono, E.; Raja, S.; Rueping, M. Complete Field Guide to Asymmetric BINOL-Phosphate Derived Brønsted Acid and Metal Catalysis: History and Classification by Mode of Activation; Brønsted Acidity, Hydrogen Bonding, Ion Pairing, and Metal Phosphates. *Chem. Rev.* **2014**, *114*, 9047–9153.
- (54) Zamfir, A.; Schenker, S.; Freund, M.; Tsogoeva, S. B. Chiral BINOL-Derived Phosphoric Acids: Privileged Brønsted Acid Organocatalysts for C–C Bond Formation Reactions. *Org. Biomol. Chem.* **2010**, *8*, 5262–5276.
- (55) Terada, M. Chiral Phosphoric Acids as Versatile Catalysts for Enantioselective Transformations. *Synthesis* **2010**, *2010*, 1929–1982.
- (56) Wang, H. Recent Advances in Asymmetric Oxidative Coupling of 2-Naphthol and Its Derivatives. *Chirality* **2010**, *22*, 827–837.
- (57) Wang, D.; Désaubry, L.; Li, G.; Huang, M.; Zheng, S. Recent Advances in the Synthesis of C2-Functionalized Pyridines and Quinolines Using N-Oxide Chemistry. *Adv. Synth. Catal.* **2021**, *363*, 2–39.
- (58) *Heterocyclic N-Oxides*; Larionov, O. V., Ed.; Springer, 2017.
- (59) For a recent report on the use of 2-methylazine N-oxides in benzylic amination reactions, see: Liman, M.; Türkmen, Y. E. Development of One-Pot Benzylic Amination Reactions of Azine N-oxides. *Tetrahedron Lett.* **2018**, *59*, 1723–1727.
- (60) Schweitzer-Chaput, B.; Sud, A.; Pintér, Á.; Dehn, S.; Schulze, P.; Klusmann, M. Synergistic Effect of Ketone and Hydroperoxide in Brønsted Acid Catalyzed Oxidative Coupling Reactions. *Angew. Chem., Int. Ed.* **2013**, *52*, 13228–13232.
- (61) Cho, K.; Leeladee, P.; McGown, A. J.; DeBeer, S.; Goldberg, D. P. A High-Valent Iron–Oxo Corrolazine Activates C–H Bonds via Hydrogen-Atom Transfer. *J. Am. Chem. Soc.* **2012**, *134*, 7392–7399.
- (62) Bryant, J. R.; Mayer, J. M. Oxidation of C–H Bonds by ((bpy)<sub>2</sub>(py)Ru<sup>IV</sup>O)<sup>2+</sup> Occurs by Hydrogen Atom Abstraction. *J. Am. Chem. Soc.* **2003**, *125*, 10351–10361.
- (63) Klingenberg, B.; Vannice, M. A. Influence of Pretreatment on Lanthanum Nitrate, Carbonate, and Oxide Powders. *Chem. Mater.* **1996**, *8*, 2755–2768.
- (64) Levan, T.; Che, M.; Tatibouet, J. M.; Kermarec, M. Infrared Study of the Formation and Stability of La<sub>2</sub>O<sub>2</sub>CO<sub>3</sub> during the Oxidative Coupling of Methane on La<sub>2</sub>O<sub>3</sub>. *J. Catal.* **1993**, *142*, 18–26.
- (65) Kim, C. H.; Li, W.; Dahlberg, K. A. Method and Architecture for Oxidizing Nitric Oxide in Exhaust Gas from Hydrocarbon Fuel Source with a Fuel Lean Combustion Mixture. US Patent US7, 964, 167 B2, 2011.
- (66) Xiang, M.; Xin, Z.-K.; Chen, B.; Tung, C.-H.; Wu, L.-Z. Exploring the Reducing Ability of Organic Dye (Acr<sup>+</sup>-Mes) for Fluorination and Oxidation of Benzylic C(sp<sup>3</sup>)-H Bonds under Visible Light Irradiation. *Org. Lett.* **2017**, *19*, 3009–3012.
- (67) Seo, S.; Slater, M.; Greaney, M. F. Decarboxylative C–H Arylation of Benzoic Acids under Radical Conditions. *Org. Lett.* **2012**, *14*, 2650–2653.
- (68) Periasamy, M.; Shanmugaraja, M.; Reddy, P. O.; Ramusagar, M.; Rao, G. A. Synthetic Transformations Using Molecular Oxygen-Doped Carbon Materials. *J. Org. Chem.* **2017**, *82*, 4944–4948.